

## Dynamic fragmentation of melted metals upon intense shock wave loading. Some modelling issues applied to a tin target

L. SIGNOR<sup>1)</sup>, A. DRAGON<sup>2)</sup>, G. ROY<sup>1)</sup>, T. DE RESSÉGUIER<sup>3)</sup>,  
F. LLORCA<sup>1)</sup>

<sup>1)</sup> *Commissariat à l'Energie Atomique  
Centre de Valduc  
21120 Is-sur-Tille, France*

<sup>2)</sup> *Laboratoire de Mécanique et Physique des Matériaux (UMR 6617)  
ENSMA – CNRS  
1 av. Clément Ader  
86961 Chasseneuil Futuroscope Cedex, France*

<sup>3)</sup> *Laboratoire de Combustion et Détonique (UPR 9028)  
ENSMA – CNRS  
1 av. Clément Ader  
86961 Chasseneuil Futuroscope Cedex, France*

WE ARE INTERESTED in the dynamic fragmentation event produced in shock-melted metals called micro-spalling. Global energetic approach is briefly reviewed. It provides a general modelling framework that leads to realistic fragment-size predictions. But the actual physical mechanisms involved remain poorly understood. We attempt to explore the conditions under which cavitation, i.e. nucleation and growth of microvoids, may be responsible for fragmentation. This cavitation process is described by means of a hollow sphere model whose matrix is made of liquid tin.

**Key words:** dynamic fragmentation, liquid metals, cavitation, hollow sphere, shock-induced melting, tin.

### 1. Introduction

WHEN A PRESSURE WAVE produced by high-velocity impact, high-explosive detonation or laser irradiation reflects from the free surface of a metallic sample, strong tensile stresses are generated and can lead to the well-known spallation fracture by nucleation, growth and coalescence of voids (ductile behaviour) or cracks (brittle behaviour). In the case of intense shock-wave loading the metal is melted (see Fig. 1, left); then, due to the relative loss of dynamic tensile strength, a fragmentation process takes place in the liquid state. According to the schematic illustration of this process given in Fig. 1 (right), the fragmented

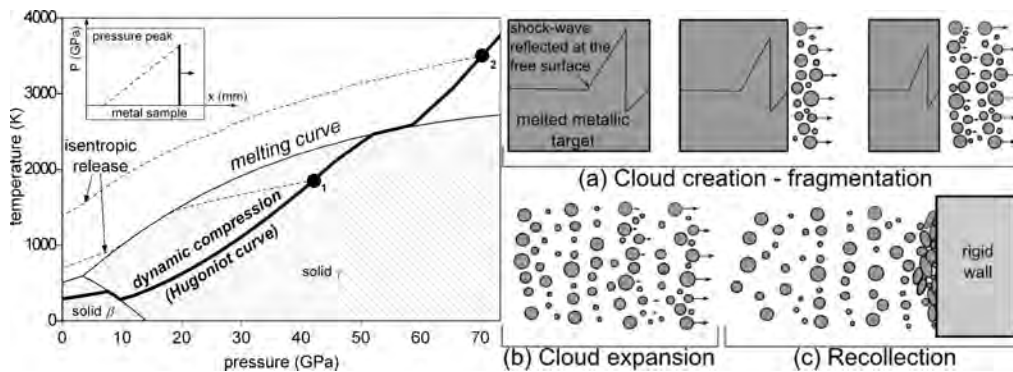


FIG. 1. Pressure–Temperature phase diagram of tin derived from BUY *et al.* [3] and MABIRE [12] (left). The states reached upon shock compression lie on the Hugoniot curve (thick solid line); isentropic release paths from states 1 and 2 are plotted in dotted lines. Melting may be achieved in release (1) or on compression (2). Schematic illustration of the target evolution after micro-spall initiation: fragmentation (a), expansional flight of the debris cloud (b), then impact on a distant wall (c) (right).

liquid metal expands as a low-density cloud of fine droplets which may later impact a distant wall.

Spallation and dynamic fragmentation of solids have been widely studied in the past, both theoretically and experimentally. An overview of these works is given by DAVISON *et al.* [5] and ANTOUN *et al.* [2]. Comparatively very scarce data can be found as yet about how the failure and fragmentation process evolves when the sample has been previously melted. Experimental evidence of such a phenomenon has been performed by ANDRIOT *et al.* [1] where it has been referred to as microspalling. More recently it has been observed on tin (HOLTKAMP *et al.* [10]) and on lead (ZHIEMBETOV *et al.* [20]) submitted to explosive loadings. An experimental investigation of microspall in tin samples under laser-driven shocks has been performed by DE RESSÉGUIER *et al.* [13]. Time-resolved velocity measurements and flash-radiography are usually performed during such experiments and provide global information and large-scale images of the debris cloud. But neither the detailed structure of the cloud nor the physical mechanisms responsible for its creation are totally understood.

The preliminary theoretical investigations presented in this paper are part of a current program aiming at physically and thermodynamically consistent modelling of the micro-spalling process (i.e. creation, expansion and re-collection of the debris cloud, see Fig. 1, right). They focus on modelling of the dynamic fragmentation of liquid metals (phase (a) in Fig. 1, right) and are applied to tin for quantitative illustration. Global energetic approaches provide a general modelling framework that can produce realistic fragment-size predictions. An example of such an approach is briefly reassessed in Sec. 2. However, global

energy balance does not bring any information concerning the actual mechanisms involved in this fragmentation process. An attempt to identify and describe those mechanisms is presented next (Sec. 3). Assuming that cavitation leads to fragmentation, the cavitation stages, namely nucleation and growth of a voids population, are described by means of the problem of a hollow sphere whose matrix is made of melted metal and submitted to a prescribed expansion. The corresponding results are further discussed in Sec. 4, where the cavitation fragmentation regime is quantified and where some thermodynamic aspects (dissipation) are considered.

## 2. Global energetic approach for dynamic fragmentation

### 2.1. Model formulation

Global energetic approach is here considered in order to provide fragment-size predictions, which are crucial for further investigation of the cloud impact process (phase (c) in Fig. 1, right). This approach has been discussed in details by GRADY [9] and applied to spallation and dynamic fragmentation of both the solid (brittle or ductile) and liquid media.

A liquid domain is considered, submitted to a uniform expansion defined by a constant dilatation rate  $D = -\dot{\rho}/\rho$ . Fragmentation is assumed to occur when the available energy becomes greater than the energy required to create fragments of diameter  $s$  and to be dissipated in this manner. This statement is written by GRADY [9] as an inequality which involves the physical properties of liquids listed in Table 1 in case of tin:

$$(2.1) \quad U + T \geq \Phi_\Gamma + \Phi_v$$

with

$$(2.2) \quad U = \frac{1}{2} K D^2 t^2, \quad T = \frac{1}{120} \rho D^2 s^2, \quad \Phi_\Gamma = 6\gamma/s, \quad \Phi_v = \eta D,$$

where  $U$  stands for the potential elastic energy density regarding volumetric expansion with the strain rate  $D$  (the material being carried into tension

**Table 1. Physical properties of liquid tin used for numerical application of global energetic approach (Sec. 2) and hollow sphere study (Sec. 3).**

Property	Symbol	Value	Unit
Reference mass density	$\rho_0$	6500	$\text{kg} \cdot \text{m}^{-3}$
Bulk modulus	$K$	40	GPa
Bulk speed of sound	$c_0 = \sqrt{K/\rho_0}$	2480	$\text{m} \cdot \text{s}^{-1}$
Surface tension	$\gamma$	0.5	$\text{N} \cdot \text{m}^{-1}$
Dynamic (Newtonian) viscosity	$\eta$	$10^{-3}$	$\text{Pa} \cdot \text{s}$

$P = -KDt$ ).  $T$  is the fraction of the total kinetic energy actually available for fragmentation. This fraction of the total amount of kinetic energy has been considered by GRADY [8] who defined it as the local kinetic energy.  $\Phi_F$  denotes the energy associated with the creation of new surfaces and is proportional to the surface energy  $\gamma$  currently identified as the surface tension in the case of liquids. Viscosity dissipation  $\Phi_v$  appears to play no significant role in Eq. (2.1) for liquid metals whose viscosity  $\eta$  is about  $10^{-3}$  Pa·s.

The upper bound for fragment of the size  $s$  at time  $t$  is given through a horizon condition:

$$(2.3) \quad s \leq 2c_0t.$$

Assuming an energy-limited fragmentation, inequalities (2.1) and (2.3) are replaced by equalities. If viscous dissipation is neglected, one obtains simple analytical expressions for fragment size  $s$ , critical tension  $P_s$  and time to failure  $t_s$ :

$$(2.4) \quad s = \left( \frac{45\gamma}{\rho_0 D^2} \right)^{1/3}, \quad P_s = \left( \frac{45}{8} \rho_0^2 c_0^2 \gamma D \right)^{1/3}, \quad t_s = \frac{1}{c_0} \left( \frac{45\gamma}{8\rho_0 D^2} \right)^{1/3}.$$

## 2.2. Numerical application and discussion

Realistic critical stress  $P_s$  and fragment-size  $s$  are predicted (Fig. 2, left). The latter is compared to scanning electron microscopy observations of tin droplets recovered after laser-shock experiments (Fig. 2, right) where dilatation rate  $D$  is estimated from  $10^7$  to  $10^8$  s $^{-1}$ . The theoretical predictions match the observed fragment-sizes that range from 1 to 10 micrometers. Additional efforts have to

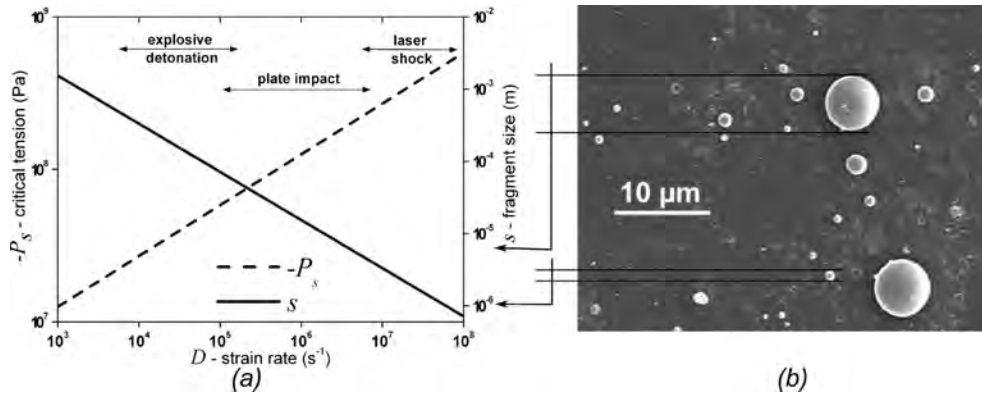


FIG. 2. (a) Fragment-size  $s$  and critical tensile stress  $P_s$  derived from Eq. (2.4) for properties of liquid tin reported in Table 1. (b) Tin droplets generated upon laser shock then re-solidified on polycarbonate shield. The detailed experimental setup is described by DE RESSÉGUIER *et al.* [13].

be pursued to acquire more precise experimental data about fragments sizes. Recent work by SIGNOR *et al.* [17] is concerned with this problem.

Time to failure  $t_s$  ranges from 0.14 ns ( $D = 10^8 \text{ s}^{-1}$ ) to 60 ns ( $D = 10^4 \text{ s}^{-1}$ ). These values are particularly small. Actually one should mention that  $t_s$  does not correspond to the moment when complete fragmentation is achieved, it defines rather the time when fragmentation becomes energetically possible. More time may be required during which irreversible mechanisms will lead to entire fragmentation and the stored energy available will be dissipated.

The above global approach does not describe the fragmentation phenomenon at a microscopic level. Energy terms expressed in Eqs. (2.1)–(2.2), especially viscous dissipation, are only a rough approximation of this complex dissipative process. In the next section we attempt to identify and describe more precisely the actual physical mechanisms involved during the fragmentation process.

### 3. Dynamic cavitation of melted metals. Hollow sphere scheme

#### 3.1. Introduction

**3.1.1. Motivations.** Experimental results of STEBNOVSKII [18] and ZHIEMBETOV *et al.* [20] indicate that fragmentation in liquids is achieved through a cavitation process, i.e. nucleation and growth of a whole voids population that reaches a critical volume fraction (or porosity  $f \sim 0.6 - 0.8$ ). Here we attempt to determine whether the initial porosity (that results from micro-voids or bubbles) can increase significantly and lead to fragmentation of a liquid metal subjected to strong impulsive loading. The ultimate stage of fragmentation is assumed to occur during a geometric coalescence process that appears when voids enter into contact. Thus if cavitation is actually responsible for fragmentation, we can establish a fragmentation criterion based on a critical porosity  $f_c$  estimated between 0.6 and 0.8. Remember that a similar cavitation process is also observed during spallation of ductile metals (see [2, 5, 16]), i.e. materials that exhibit fluid-like properties.

We attempt to describe this complex cavitation process, i.e. voids growth, in a simplified manner through the problem of a hollow sphere in expansion. The main question to be answered is: *according to a given prescribed loading, does the porosity reach a sufficient level to admit that cavitation is responsible for fragmentation?*

**3.1.2. Physical meaning of the hollow sphere model.** The hollow sphere model has been widely used to model shock-induced effects such as dynamic compaction of porous media [4] and especially ductile damage and fracture by spallation [11, 16]. The present work is an attempt to explore the ability of such a model to provide quantitative data about the cavitation process in melted materials.

The main hypothesis underlying this modelling scheme is that the hollow sphere pattern is assumed to be representative of voids growth in a volume  $V$  within the sample, where kinematical and thermodynamical state is sufficiently uniform (Fig. 3). This tacitly implies that all voids in the sub-domain  $V$  evolve in the same manner.

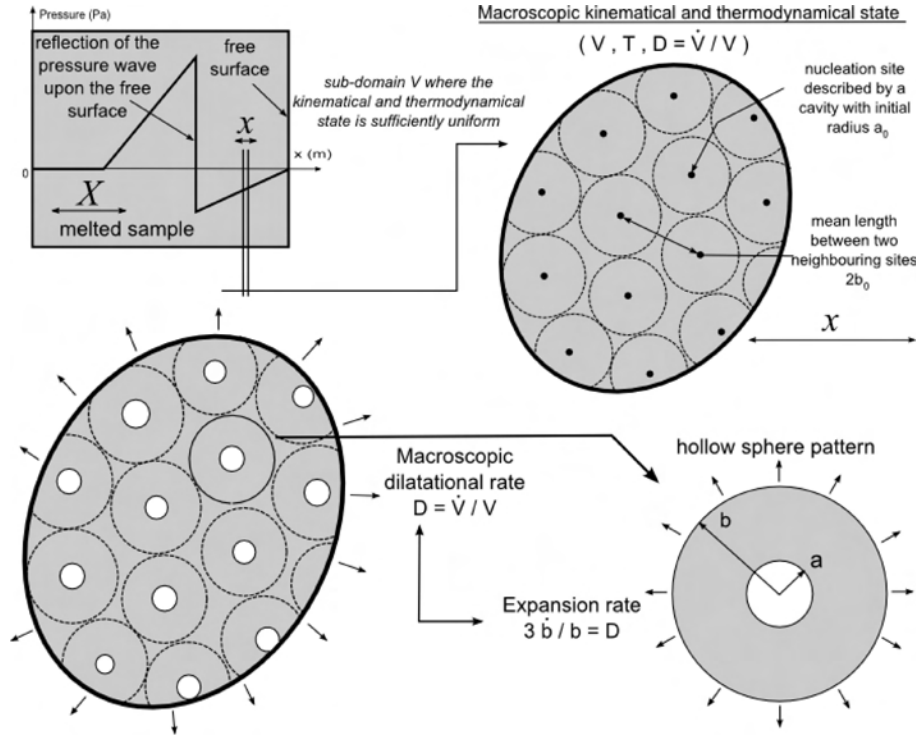


FIG. 3. Illustration of hypotheses underlying the hollow sphere model applied to the description of the micro-spalling fragmentation phenomenon.

We consider a hollow sphere with internal and external radii, respectively denoted  $a$  and  $b$  in the current configuration ( $a_0$  and  $b_0$  in the reference initial one). With respect to the hypothesis expressed above and illustrated in Fig. 3,  $b_0$  can be interpreted as the mean half-length between two neighbouring activated sites. With this definition of  $b_0$ , the ratio  $f = a^3/b^3$  stands for the actual (or physical) porosity, i.e. voids volume fraction. These sites are initial defects or local heterogeneities where voids are nucleated during the first stage of expansion. Although the data concerning microscopic state of shock-melted metals are still scarce, it seems that thermal inhomogeneities may play the role of potential sites of cavitation. According to this interpretation  $b_0$  would probably be affected by strain-rate or shock-pressure. But such investigation

lies outside the scope of the present paper, limited to a parametric study over a large range of  $b_0$ . The obtained results will be discussed with respect to this interpretation for  $b_0$ . The initial internal radius  $a_0$  is not attached to a physical void initially present in the melted metal. But singular effects (due to viscosity in particular) do not allow to choose  $a_0 = 0$  in the framework of the hollow sphere model. Instead,  $a_0$  is chosen in such a way that the initial porosity  $f_0$  is sufficiently small so that the material can be considered as initially intact.

Actually this modelling suggests the existence of three distinct length scales as illustrated in Fig. 3.  $X$  denotes the characteristic length of the target and/or the pressure wave. Actually, the sample (or target) has to be considered as a structure whose length scale is defined by  $X$ . The second length scale  $x$  defines the domain where the applied loading can be assumed to be approximately uniform. This volume is also supposed to contain a great number of defects or nucleation sites spaced about  $b_0$ . Separation scale rule rigorously implies that  $b_0 \ll x \ll X$ . This is greatly restrictive in the case of strong transient loading like shock-waves because  $x$  may be of the order of structural defects, i.e. of  $b_0$ . Such considerations have to be pointed out but their rigorous examination lies beyond the scope of the present work. These questions have been discussed in details by DRAGON and TRUMEL [7], in the context of application regarding spallation damage of ductile metals.

**3.1.3. Description of the cavitation process.** Hollow sphere expansion is decomposed here into two successive phases that lead to two distinct problems. During *phase 1* ( $0 \leq t \leq \tau$ ), the hollow sphere is subjected to the applied loading which consists in a constant macroscopic dilatation rate  $D$  prescribed on the outer boundary (Table 2). During *phase 2* ( $t > \tau$ ), the hollow sphere evolves in free inertial expansion due to the kinetic energy acquired during *phase 1*.

**Table 2. Typical shock loading parameters.**

Loading No.	1	2
Corresponding experimental configuration	plate impact	laser shocks
Dilatation rate $D$ ( $\text{s}^{-1}$ )	$10^6$	$10^8$
Loading duration $\tau$ (s)	$2 \cdot 10^{-7}$	$2 \cdot 10^{-9}$

For the sake of simplicity, the applied loading is defined by only two constant scalar parameters (dilatation rate  $D$  and duration  $\tau$ ) which are expected to represent the dynamic conditions encountered in application. The present study is restricted to two sets  $(D, \tau)$  reported in Table 2. Each one is associated

with a typical shock experiment for which approximative length scale  $X$  can be assessed. Millimetric samples are usually used in plate impact experiments (loading case No. 1), whereas laser shocks (loading case No. 2) are performed on targets of a few hundreds micrometers in thickness.

One should mention that the actual loading, to which a material element within the target is subjected, results from waves interaction and may be affected by stress relaxation induced by voids growth. The choice of the suitable loading that has to be prescribed as a boundary condition to the hollow sphere pattern is not trivial for such highly dynamic events.

### 3.2. Phase 1: prescribed expansion

**3.2.1. Formulation.** Displacement field proposed by DENOVAL and DIANI [6] allows to account for homogenous dilatation state in the liquid matrix:

$$(3.1) \quad r(r_0, t)^3 = \varphi(t)[r_0^3 + \omega(t)], \quad a \leq r \leq b,$$

where  $\varphi = \rho_0/\rho$  denotes a dilatation factor and  $\omega$  stands for volume increase of the cavity. The useful kinematical quantities (e.g. velocity, acceleration and strain rate tensor  $d_{ij}$ ) are derived from Eq. (3.1).

Compressibility effect influences mainly the nucleation stage i.e. the beginning of *phase 1*;  $a_0$  is chosen very small (but not zero) so avoiding non-physical singularities. But as it is stated below, compressibility does not affect further porosity evolution as long as  $b_0$  is sufficiently small.

The hollow sphere matrix is supposed to be a compressible and viscous liquid which stands for melted tin. Its constitutive equation results from the stress tensor partition into an isotropic/conservative part (pressure) and a deviatoric/dissipative part (Newtonian viscous stress), i.e.  $\sigma_{ij} = -P\delta_{ij} + \tau_{ij}$ . With the displacement field in Eq. (3.1), one obtains:

$$(3.2) \quad \begin{aligned} \sigma_{ij} &= K \ln \left( \frac{\rho_0}{\rho} \right) \delta_{ij} + 2\eta \left( d_{ij} - \frac{1}{3} d_{kk} \delta_{ij} \right) \\ &= K \ln \varphi \delta_{ij} + \frac{4}{3} \eta \frac{\varphi \dot{\omega}}{r^3} \begin{pmatrix} -1 & 0 & 0 \\ 0 & 1/2 & 0 \\ 0 & 0 & 1/2 \end{pmatrix}. \end{aligned}$$

The spatial (Eulerian) form of the equation of balance of linear momentum is written with respect to the spherical symmetry of the present problem:

$$(3.3) \quad \frac{\partial \sigma_{rr}}{\partial r} + \frac{2}{r}(\sigma_{rr} - \sigma_{\theta\theta}) = \rho \ddot{r}.$$

By using the constitutive relation (3.2), Eq. (3.3) is integrated from  $a$  to  $b$  with a traction-free boundary at  $r(t) = a(t)$ :

$$(3.4) \quad K \ln \varphi = \frac{4}{3} \eta \frac{\dot{\omega}}{a_0^3 + \omega} + \int_a^b \rho \ddot{r} dr.$$

The detailed expression for  $\int_a^b \rho \ddot{r} dr$  does not appear in Eq. (3.4) but can be derived from Eq. (3.1).

The velocity  $\dot{b}$  at  $r(t) = b(t)$  is connected with a given macroscopic dilatation rate  $D$ :

$$(3.5) \quad D = 3 \frac{\dot{b}}{b} = \frac{\dot{\omega}}{b_0^3 + \omega} + \frac{\dot{\varphi}}{\varphi}.$$

Initial conditions of the problem are  $\varphi(0) = 1$ ,  $\omega(0) = 0$ ,  $\dot{\varphi}(0) = D$  and  $\dot{\omega}(0) = 0$ . One notices that the hollow sphere is not initially at rest. The initial conditions have to be compatible with the boundary condition (3.5) which requires a non-zero initial velocity. The choice  $\dot{\varphi}(0) = D$  and  $\dot{\omega}(0) = 0$  corresponds to the instantaneous response due to the bulk elasticity of the liquid matrix.

**3.2.2. Results.** After solving the differential equations system (3.4)–(3.5), one can compute from  $\omega(t)$  and  $\varphi(t)$  the “macroscopic” pressure  $P_{macro} = -\sigma_{rr}(b, t)$  and the porosity  $f = a(a_0, t)^3/b(b_0, t)^3$ .

Examples of evolution of these quantities during the beginning of the prescribed expansion (*phase 1*) are given in Fig. 4 for loading case No. 1. An

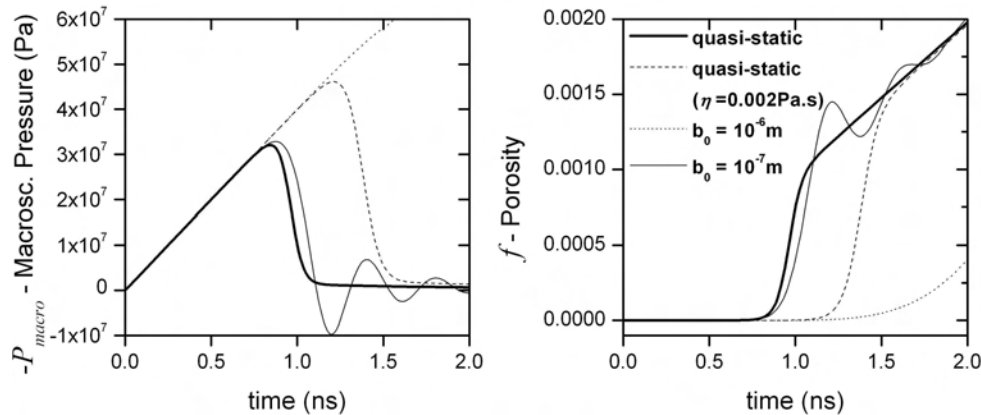


FIG. 4. Evolution of the macroscopic pressure (left) and porosity (right) during the beginning of the hollow sphere expansion. These results are obtained with the properties of liquid tin in Table 1 (except the dashed curves that correspond to  $\eta = 2.10^{-3}$  Pa.s) and with the dilatation rate of loading No. 1 in Table 2.

important feature of this stage can be observed when inertial effects are negligible or neglected, i.e. when  $\int_V \rho \ddot{r} dv = 0$  in Eq. (3.4). These cases are referred to as quasi-static in Fig. 4. During the first stage of expansion, liquid matrix stores elastic energy without increase of the void size. Then one observes a significant growth of cavity size (and of corresponding porosity) followed by a pressure drop. In quasi-static regime the cavity “explodes” for the maximal pressure attained  $P_c = -\sigma_{rr}(b, t_c) = P_{macro}(t_c)$  with  $\dot{P}_{macro}(t_c) = 0$ . This strong increase of the cavity size may be seen as the true cavitation incipience. This phenomenon occurs rapidly and largely before the end of the applied loading ( $t_c \ll \tau$ ). Finally, the cavity growth supports alone the prescribed expansion: porosity evolution is comparable to the one obtained for an incompressible displacement field. As illustrated in Fig. 4, viscous stress has a stabilizing effect that leads to a delay of the explosion mentioned above.

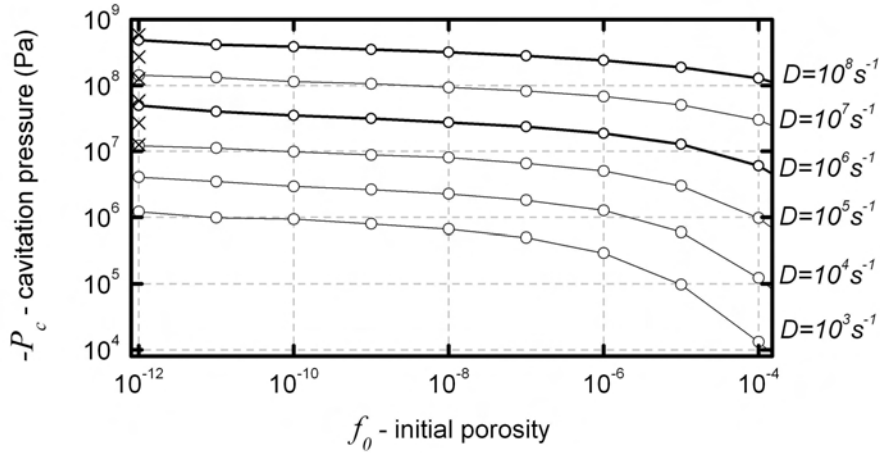


FIG. 5. Quasi-static cavitation pressure  $P_c$  as a function of prescribed dilatation rate  $D$  and initial porosity  $f_0$ . These results are obtained with the physical properties (reference mass density  $\rho_0$ , bulk modulus  $K$  and dynamic viscosity  $\eta$ ) of liquid tin reported in Table 1. The two reference loadings indicated in Table 2 considered in this paper correspond to the two thick curves.

Quasi-static cavitation pressure  $P_c$  has been computed for a large range of dilatation rate  $D$  and initial porosity  $f_0$ . The results, obtained with the physical properties of liquid tin (Table 1), are reported in Fig. 5. Although cavitation pressure cannot be defined for a strictly intact liquid ( $P_c$  does not reach a plateau when  $f_0 \rightarrow 0$ ) it can be estimated, at a given dilatation rate  $D$ , by the mean value taken over a range of low initial porosity, e.g. from  $10^{-12}$  to  $10^{-10}$ . The resulting values lie between 10 and 1000 MPa. Cavitation pressure may be seen as a threshold at which the failure mechanisms are initiated. In this way the

obtained values seem realistic in comparison to Grady's critical pressures  $P_s$  which are shown as crosses in Fig. 5.

When inertial effects are taken into account and not negligible, the cavity growth is slowed down and accompanied by oscillations around the incompressible evolution. Such effect is mainly governed by  $b_0$  which defines the total amount of mass involved in each cavitation pattern. For  $b_0 \leq 10^{-7}$  m quasi-static and dynamic solutions are quite similar (solid curves in Fig. 4). This is not at all the case for  $b_0 \geq 10^{-6}$  m (Fig. 4 and Fig. 6, left) because oscillations become important and are not damped by viscous stress. But when porosity evolution is observed for a time scale of the order of  $\tau$  (Fig. 6, right), all the curves evolve in a similar way, i.e. close to incompressible solution, and oscillations may be neglected. Thus we can assume that the further evolution of porosity in free inertial expansion during *phase 2* for  $t \geq \tau$  occurs in an incompressible regime. This corresponds to a particular case of the displacement field given in Eq. (3.1) with  $\varphi = 1$ . Furthermore we will assume that the initial conditions for the problem of *phase 2* are given by the incompressible solution of the problem of *phase 1* at  $t = \tau$ . This incompressible solution defines the global tendency around which the computed compressible solutions oscillate as shown in Fig. 6. In the following these assumptions are referred to as the "incompressibility" hypothesis. This hypothesis is not valid any more when  $b_0$  becomes greater than about  $5 \cdot 10^{-5}$  m for loading case No. 1 (an example is given for  $b_0 = 10^{-4}$  m that corresponds to the dashed curve in Fig. 6, right) or greater than about  $10^{-6}$  m for loading case No. 2. In these cases the induced oscillations become so important that

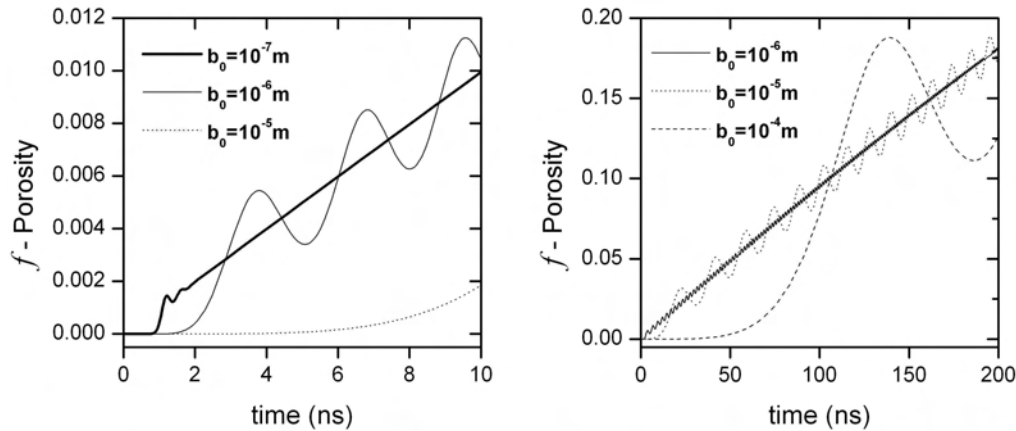


FIG. 6. Porosity evolution during *phase 1* for liquid tin (physical properties listed in Table 1), loading case No. 1 (Table 2) and  $b_0$  ranging from  $10^{-7}$  to  $10^{-4}$  m. On the left, only the beginning of the prescribed loading is visible ( $0 \leq t \leq 0.05\tau$ ). On the right, all the loading duration is shown ( $0 \leq t \leq \tau$ ).

the cavity growth significantly differs from the incompressible one. For extreme values of  $b_0$  (higher than  $10^{-4}$  m for loading No. 1 and  $3 \cdot 10^{-6}$  m for loading No. 2), cavity hardly begins to grow for the loading time interval  $\tau$  due to inertial resistance. These values correspond to the cases where  $b_0$  is of the order of  $X$ , i.e. the characteristic length scale of the sample (Fig. 3). Separation scale rule is not satisfied any more.

When the ‘‘incompressibility’’ hypothesis is valid, the porosity reached at  $t = \tau$  is about 0.2, that is less than the critical value  $f_c$  ( $\sim 0.6 - 0.8$ ) at which fragmentation is assumed to occur. Thus, the crucial question to answer is now: owing to the kinetic energy acquired during the *phase 1* (which is mainly governed by  $b_0$ ), does the porosity reach the critical value during the *phase 2*?

### 3.3. Phase 2: inertial expansion

**3.3.1. Formulation.** According to the conclusions established in the previous section for *phase 1*, we reformulate here a second hollow sphere problem.

The new displacement field is the incompressible counterpart of Eq. (3.1) with  $\varphi = 1$ ,

$$(3.6) \quad r(r_0, t)^3 = r_0^3 + \omega(t).$$

The new boundary conditions are prescribed as a form of traction given at the inner and outer radii. Actually this is the second reason that explains why the *phase 2* is treated with an incompressible displacement field. Indeed the compressible one (3.1) is not appropriate to the boundary value problem with two prescribed tractions. As *phase 2* corresponds to a free expansion,  $r = b$  is a traction-free boundary. At  $r = a$  the prescribed traction stands for surface tension effects. Surface tension has been neglected during *phase 1* because the initial ‘nucleus’ cavity introduced within the hollow sphere pattern does not represent a physical cavity initially contained in the melted metal. Thus, assigning surface tension effects to this initial cavity has no physical meaning and might prematurely lead to its collapse. But it is difficult to state when the cavity becomes a ‘physical’ cavity and when the surface tension effects have to be taken into account. Consequently, they have been disregarded during *phase 1*. This choice is equivalent to considering the whole *phase 1* as a sort of prolonged nucleation. For the *phase 2* related to inertial expansion the boundary conditions are:

$$(3.7) \quad \sigma_{rr}(r = b, t) = 0, \quad \sigma_{rr}(r = a, t) = 2\gamma/a.$$

Equation of motion is integrated between  $a$  and  $b$ :

$$(3.8) \quad \sigma_{rr}(r = b, t) - \sigma_{rr}(r = a, t) + \int_a^b \frac{2}{r} (\sigma_{rr} - \sigma_{\theta\theta}) dr = \int_a^b \rho \ddot{r} dr.$$

One finally obtains the following second-order ordinary differential equation in  $\omega$ :

$$(3.9) \quad -\frac{2\gamma}{a} + \frac{4}{3}\eta\dot{\omega} \left( \frac{1}{a^3} - \frac{1}{b^3} \right) = \rho_0 \left[ \frac{\ddot{\omega}}{3} \left( \frac{1}{a} - \frac{1}{b} \right) + \frac{\dot{\omega}^2}{18} \left( \frac{1}{b^4} - \frac{1}{a^4} \right) \right].$$

The new initial conditions at  $t = \tau$  result from the incompressible solution  $\omega_*$  to the hollow sphere problem for *phase 1*. It is obtained by solving Eq. (3.5) with  $\varphi = 1$  and  $\dot{\varphi} = 0$  as follows:

$$(3.10) \quad \omega_*(\tau) = b_0^3 [\exp(D\tau) - 1], \quad \dot{\omega}_*(\tau) = b_0^3 D \exp(D\tau).$$

**3.3.2. Results.** Porosity evolution is explored for the physical properties of liquid tin (Table 1), for the two reference loading cases (Table 2) and for  $b_0$  ranging from  $10^{-8}$  to  $10^{-4}$  m. After  $t = \tau$  the cavity size and porosity continue to increase and reach their maximum values when viscosity and surface tension effects have consumed the kinetic energy available, as illustrated in Fig. 7 (left). Then the cavity may collapse due to surface tension.

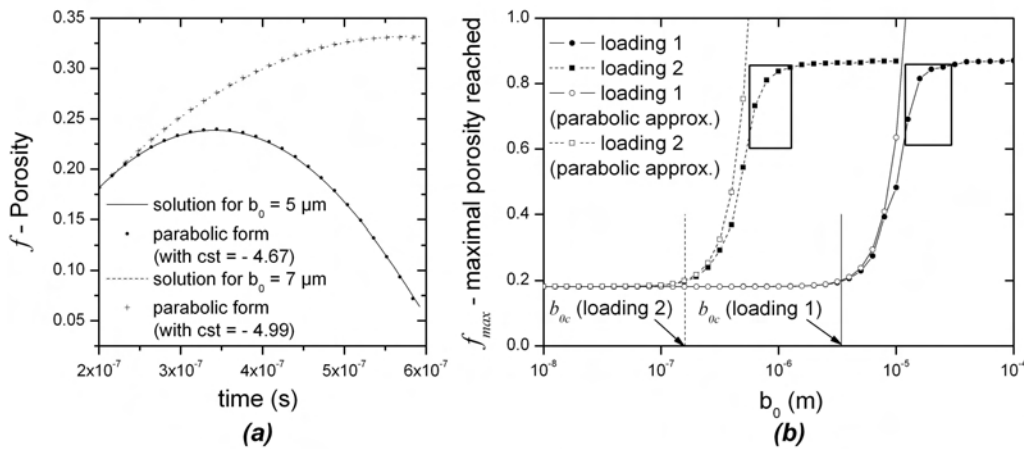


FIG. 7. Free inertial expansion of the hollow sphere (*phase 2*). On the left, examples of porosity evolution after  $t = \tau$  for the loading case No. 1 (Table 2) and the corresponding approximation using the parabolic form described in Appendix A. On the right is displayed the maximal porosity reached for the respective loading cases and the values of  $b_0$ . The computed results (filled symbols) and those derived from the parabolic approximation (empty symbols) show a good agreement for the lower values of  $b_0$ .

This behaviour is mainly governed by  $b_0$ . On the Fig. 7 (right) the maximal porosity reached (or porosity achieved at  $t = 10\tau$  if no maximum is encountered before) for varying  $b_0$  is reported. Three domains can be distinguished. (i) The *non-cavitation regime* is observed for low  $b_0$  values ( $b_0 \leq b_{0c}$ ). Porosity does

not evolve because cavity collapses almost instantaneously. The maximal porosity  $f_{max}$  is close to porosity at  $t = \tau$ . (ii) During the *transition regime*  $f_{max}$  increases progressively with  $b_0$ . (iii) In the *cavitation fragmentation regime*  $f_{max}$  systematically exceeds 0.8 before  $t = 10\tau$ . These conclusions are observed for both loading cases. The curves in Fig. 7 (right) are shifted towards lower values of  $b_0$  when the dilatation rate increases.

An analytical criterion that predicts  $b_{0c}$ , i.e. the separation between the *non-cavitation regime* and the *transition regime*, can be established. It is derived from a parabolic form that aims to fit the computed porosity evolution during *phase 2*. The details of this calculation are reported in Appendix A. The corresponding results are included in Fig. 7.

Finally one should remind that neither the "incompressibility" assumption nor the separation scale rule are valid for the highest  $b_0$  values. The corresponding maximal porosities reported in Fig. 7 must be disregarded because, actually, cavitation may not reach a significant amount of void volume fraction in such cases. On the other hand, very low  $b_0$  values have also been explored. The framework of continuum mechanics for this length scale may be a debatable point.

## 4. Discussion

### 4.1. Role of cavitation in fragmentation

Cavitation in a liquid subjected to intense dynamic expansion has been investigated by means of the hollow sphere model in order to assess if cavitation may be responsible for fragmentation. A particular attention is paid to the parameter  $b_0$  (outer radius of the hollow sphere that stands for the half-length between two activated sites of cavitation) which preponderantly influences the cavitation process. Based on the study of the two cavitation stages (*phases 1* and *2*), the domain, for which one can assert that cavitation is responsible for fragmentation ( $f_{max} \geq f_c \sim 0.6 - 0.8$ ), is defined for each loading by rectangles in Fig. 7. This range of values for  $b_0$  is similar to the fragment size  $s$  predicted by the global energetic approach (Sec. 2).

Future work will concern the identification of  $b_0$ . Better understanding of the shock-induced melting process, both theoretically and experimentally, should provide data concerning the spatial distribution of the probable thermal inhomogeneities that may play the role of cavitation nuclei. Moreover, observation of recovered targets after laser-shock experiments may give new insights into the cavitation process (see DE RESSÉGUIER *et al.* [14, 15]).

Cavitation has been inferred here to be the most probable failure mechanism responsible for fragmentation. But in the framework of the hollow sphere model, any other mechanism, such as decohesion, is disregarded. Voids coalescence may

also occur prematurely (for  $f < f_c \sim 0.6 - 0.8$ ) by voids linking, e.g. through a kind of shear-banding process. A more rigorous treatment of the problem of hollow sphere expansion should have included a stability analysis which could provide some insight to predict such a phenomenon.

#### 4.2. Energy dissipation during cavitation

The cavitation process is now discussed from an energetic viewpoint aiming at establishing a link with the global energetic approach (Sec. 2). Solving of two hollow sphere problems (Sec. 3) allows to compute the total amount of energy exchanged and dissipated during the cavitation process, i.e.  $0 \leq t \leq t_m$  where  $t_m$  denotes the time when the maximal porosity is reached (or  $t_m = 10\tau$  if no maximum is encountered before  $10\tau$ ). Definitions that allow to establish the energy balance are reported in Appendix B. Here we focus on the dissipative mechanisms that accompany the cavitation process and contribute to fragmentation. These are viscous dissipation and creation of surface which are described by the quantities  $\Phi_{v(0-\tau)}$ ,  $\Phi_{v(\tau-t_m)}$  and  $\Phi_{\Gamma(\tau-t_m)}$  defined in Appendix B. This notation aims at establishing of a direct comparison with the global energetic approach by comparing the hollow sphere expansion results to the corresponding estimation of  $\Phi_v$  and  $\Phi_\Gamma$  (now denoted  $\Phi_{v(Grady)}$  and  $\Phi_{\Gamma(Grady)}$  for clarity) expressed in Eqs. (2.1)–(2.2).

The comparison at stake suggests a thermodynamic re-interpretation of the purely mechanical hollow sphere problem where the relevant energy balance may be related to the kinetic energy theorem [19]. Irreversible (viscous) stresses obviously give rise to a bulk dissipation which is denoted  $\varphi_v$ . Surface tension acts like an external force prescribed as a boundary condition to the hollow sphere pattern. But regarding the cavitating media, it corresponds to the stored energy that is recoverable as long as void growth remains stable and coalescence does not occur. When a given threshold (e.g. a critical porosity) is reached, this stored energy is dissipated during the coalescence of neighbouring voids from which the final fragments result. Thus, although the quantity  $\Phi_{\Gamma(\tau-t_m)}$  does not represent the entire dissipated energy before effective fragmentation, this notation has been adopted to put forward the link with its counterpart  $\Phi_{\Gamma(Grady)}$ .

Since the cavitation process depends on  $b_0$ , energy —  $b_0$  plots are given in Fig. 8 (loading case No. 1) and Fig. 9 (loading case No. 2). To correctly interpret these plots, it is necessary to keep in mind the conclusions established in the previous sections.

$\Phi_{v(Grady)}$  and  $\Phi_{\Gamma(Grady)}$  are also reported in Fig. 8 and Fig. 9. As concluded in Sec. 2, this estimate of viscous dissipation is largely negligible. But the present study reveals that  $\Phi_{v(Grady)}$  underestimates the actual viscous dissipation: in particular  $\Phi_{v(0-\tau)}$  is largely greater than  $\Phi_{v(Grady)}$ . Some comments are useful

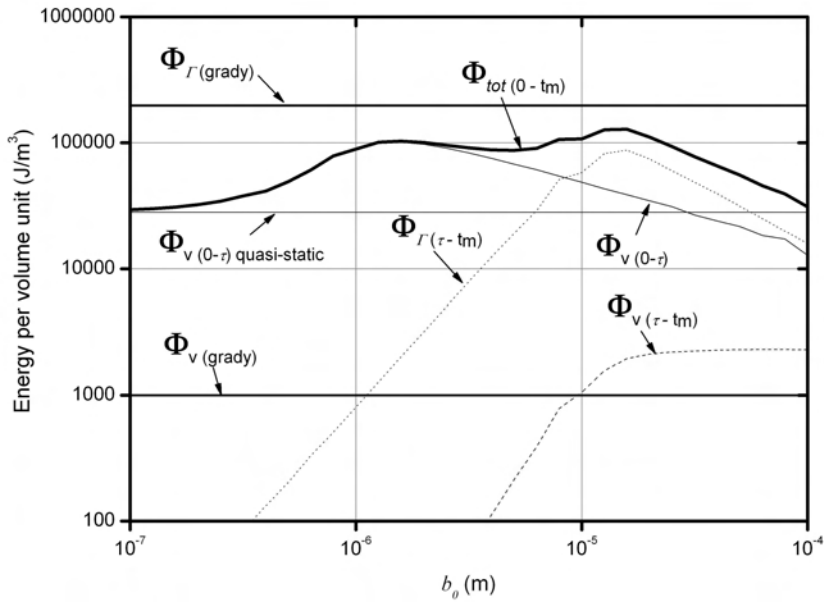


FIG. 8. Energy dissipated per unit volume during the hollow sphere expansion for loading case No. 1. The total amount of energy dissipated  $\Phi_{tot(0-t_m)}$  is divided into three parts: viscous dissipation  $\Phi_{v(0-\tau)}$  during *phase 1*, viscous dissipation  $\Phi_{v(\tau-t_m)}$  during *phase 2* and creation of surface  $\Phi_{\Gamma(\tau-t_m)}$  during *phase 2*. The corresponding values estimated in the global energetic approach are also reported as  $\Phi_{v(Grady)}$  and  $\Phi_{\Gamma(Grady)}$ .

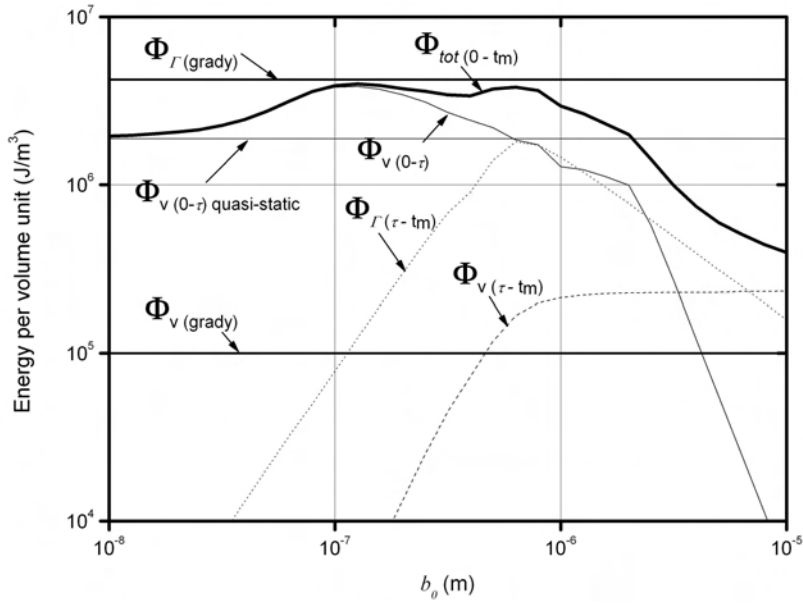


FIG. 9. A plot similar to that of Fig. 8 but for the loading case No. 2.

on  $\Phi_{v(0-\tau)}$  dependence on  $b_0$  in Fig. 8 and Fig. 9. When inertial effects are negligible ( $b_0 \rightarrow 0$ ),  $\Phi_{v(0-\tau)}$  reaches a plateau which corresponds to the quasi-static solution ( $\Phi_{v(0-\tau)} \rightarrow \Phi_{v(0-\tau) \text{ quasi-static}}$ ). As  $b_0$  increases, the induced oscillations lead to an additional amount of viscous dissipation. For larger  $b_0$  values, voids growth is slowed down and less dissipation is observed.

During *phase 2*, surface energy is predominant ( $\Phi_{\Gamma(\tau-t_m)} \gg \Phi_{v(\tau-t_m)}$ ). Before the *cavitation fragmentation regime* ( $b_0$  for which  $f_{max} \leq 0.8$  in Fig. 7), both  $\Phi_{\Gamma(\tau-t_m)}$  and  $\Phi_{v(\tau-t_m)}$  increase with  $b_0$  since the corresponding maximal porosity reached also increases. For higher  $b_0$ , the maximal porosity reached remains almost constant. As a result, since viscous dissipation is proportional to the volume of the hollow sphere, the corresponding amount of energy dissipated per unit volume  $\Phi_{v(\tau-t_m)}$  reaches a plateau. Regarding the surface energy per unit volume,  $\Phi_{\Gamma(\tau-t_m)}$  is found to be inversely proportional to  $b_0$ .

Here we focus on the range of  $b_0$  where cavitation can lead to fragmentation (domains defined by rectangles in Fig. 7). In this case  $\Phi_{v(0-\tau)}$  and  $\Phi_{\Gamma(\tau-t_m)}$  are quite comparable. But the total amount of energy  $\Phi_{tot(0-t_m)}$  remains lower than the surface energy  $\Phi_{\Gamma(Grady)}$  that results from the global energetic criterion. This is mainly due to the fact that  $\Phi_{\Gamma(\tau-t_m)}$  is an underestimate of the actual surface energy required for fragmentation. The two reasons for this are: (i) surface tension has been neglected during *phase 1* and (ii) the hollow sphere model does not account for the ultimate stage of coalescence (during which new surfaces are still created). The new estimate of viscous dissipation  $\Phi_{v(0-\tau)}$ , included in the energetic fragmentation criterion defined by Eqs. (2.1)–(2.2), does not affect significantly fragment size predictions.

## 5. Conclusion

Micro-spalling is a dynamic fragmentation phenomenon that occurs in shock-melted metals. Global energetic approach provides realistic fragment-size predictions. But the actual mechanisms involved in this fragmentation process are ignored by this global approach. In this paper we attempt to identify and describe the possible predominant mechanism. On the basis of experimental results, cavitation, i.e. nucleation and growth of voids, is assumed to be the most probable failure mechanism.

The growth of a whole voids population is described by means of the hollow sphere scheme involving two specific stages of sphere expansion. We then establish the domain for which cavitation can (or cannot) be responsible for fragmentation. The corresponding evolution is governed preponderantly by  $b_0$  which stands for the half-distance between two nucleated sites.

The hollow sphere study presented here is a preliminary modelling attempt that aims at bringing new insight into this specific fragmentation process which

needs yet to be better understood. It provides an improved and quantitative understanding about the role of cavitation during the fragmentation process. Both experimental and theoretical efforts have to be pursued to investigate furthermore this phenomenon.

### Appendix A. Non-cavitation criterion

We attempt to fit the solution of the problem 2, i.e. of the free inertial expansion (in terms of porosity evolution  $f(t)$ , illustrated in Fig. 7, left), with the following parabolic form  $F(t)$ :

$$(A.1) \quad f(t) \approx F(t) = A + Bt + Ct^2.$$

The first constraint corresponds to the initial conditions of *phase 2* at  $t = \tau$  given in Eq. (3.10). If  $f_*(t)$  denotes the porosity evolution for an incompressible hollow sphere submitted to a dilatation rate  $D$ , one obtains:

$$(A.2) \quad f_*(\tau) = 1 + (f_0 - 1) \exp(-D\tau) \approx 1 - \exp(-D\tau).$$

Thus  $F(\tau) = f_*(\tau)$  and  $\dot{F}(\tau) = \dot{f}_*(\tau)$  lead to:

$$(A.3) \quad A = f_*(\tau) - \dot{f}_*(\tau)\tau + C\tau^2, \quad B = \dot{f}_*(\tau) - 2C\tau.$$

Porosity evolution during *phase 2* results mainly from the competition between inertial effects and surface tension. Based on dimensional considerations,  $C$  is chosen to take the following form in which  $c$  is a dimensionless constant:

$$(A.4) \quad C = c \cdot \gamma / (\rho_0 b_0^3).$$

An analytical approximation  $F_{max}$  of the actual maximal porosity reached  $f_{max}$  can be defined from Eqs. (A.1)–(A.3)–(A.4):

$$(A.5) \quad f_{max} \approx F_{max} = A - \frac{B^2}{4C}.$$

A good agreement is obtained with  $c = -4.8$  for  $b_0$  values ranging from the *non-cavitation regime* to the beginning of the *transition regime* (see Fig. 7).

The criterion  $F_{max} \leq 1.1F(\tau)$  provides the domain for which cavitation does not evolve significantly after the end of the applied loading. This criterion is analytically expressed by using the approximate parabolic form established above:

$$(A.6) \quad \frac{(\rho_0 b_0^3)}{\gamma} \cdot \frac{D^2 \exp(-D\tau)}{1 - \exp(D\tau)} \leq 0.4c.$$

The critical value  $b_{0c}$  corresponds to the larger value of  $b_0$  that satisfies inequality (A.6) when the other parameters are fixed. These critical values are  $3.42 \mu m$  for loading case No. 1 and  $0.16 \mu m$  for loading case No. 2, and are indicated in Fig. 7 (right) by vertical lines.

## Appendix B. Energetic interpretation of the hollow sphere model

### B.1. Preliminary remarks

In this purely mechanical study, the energy balance corresponds to the kinetic energy theorem for the domain of the hollow sphere (see [19], p. 67):

$$(B.1) \quad \dot{T} = P_i + P_e,$$

$$(B.2) \quad T = \int_{D_t} \frac{1}{2} \rho v^2 dv,$$

$$(B.3) \quad P_i = - \int_{D_t} \sigma_{ij} d_{ij} dv,$$

$$(B.4) \quad P_e = \int_{S_t} t_i v_i ds + \int_{D_t} \rho f_i v_i dv.$$

$S_t$  (respectively  $D_t$ ) denotes the position of the boundary (the domain)  $S$  ( $D$ ) of the hollow sphere at time  $t$ .  $\dot{T}$  defines the material derivative of the kinetic energy  $T$ .

The following quantities are involved in Eq. (B.1):

- During *phase 1*: the rate of change of kinetic energy  $\dot{T}$ , the power of internal forces  $P_i$ , i.e. the rate of work of reversible stresses (pressure)  $\dot{U}$  and the rate of work of irreversible (viscous) stresses  $\varphi_v$  ( $P_i = \dot{U} + \varphi_v$ ), plus the power of external forces  $P_e$  (where body forces are neglected).
- During *phase 2*: the rate of change of kinetic energy  $\dot{T}$ , the power of internal forces  $P_i$ , i.e. the rate of work of irreversible (viscous) stresses  $\varphi_v$  ( $P_i = \varphi_v$ ) and the power of external forces  $P_e$ , which are here the effects of surface tension acting on the inner radius  $\varphi_\Gamma$  ( $P_e = \varphi_\Gamma$ ).

Here we focus on the dissipative mechanisms that accompany the cavitation process and contribute to fragmentation, i.e. viscous dissipation and creation of surface. The balance is not detailed below; only the terms related to dissipative mechanisms are developed.

### B.2. Viscous dissipation during *phase 1*

$$(B.5) \quad \varphi_v = \int_a^b -\tau_{ij} d_{ij} 4\pi r^2 dr,$$

where  $\tau_{ij}$  and  $d_{ij}$  can be deduced from Eq. (3.2).

In order to compare this quantity with the estimate expressed in Eqs. (2.1)–(2.2), the total amount of energy dissipated during *phase 1* is computed per unit volume, according to the following expression:

$$(B.6) \quad \Phi_{v(0-\tau)} = \int_0^\tau \frac{\varphi_v}{V} dt,$$

where  $V = \frac{4}{3}\pi b^3$  is the total volume of the hollow sphere.

### B.3. Viscous dissipation and creation of surface during *phase 2*

$$(B.7) \quad \varphi_v = \int_a^b -\tau_{ij} d_{ij} 4\pi r^2 dr, \quad \varphi_\Gamma = \frac{2\gamma}{a} v_r(a, t) 4\pi a^2$$

where  $v_r$  is derived from Eq. (3.6):

$$(B.8) \quad v_r(r, t) = \frac{\dot{\omega}(t)}{3r^2}.$$

The corresponding rates are integrated per unit volume between  $\tau$  and  $t_m$  (time when the maximal porosity is reached or  $t_m = 10\tau$  if no maximum is encountered before):

$$(B.9) \quad \Phi_{v(\tau-t_m)} = \int_\tau^{t_m} \frac{\varphi_v}{V} dt, \quad \Phi_{\Gamma(\tau-t_m)} = \int_\tau^{t_m} \frac{\varphi_\Gamma}{V} dt.$$

## References

1. P. ANDRIOT, P. CHAPRON, V. LAMBERT, F. OLIVE, *Influence of melting on shocked free surface behaviour using Doppler laser interferometry and X-ray densitometry*, [in:] *Shock Waves in Condensed Matter*, J.R. ASAY, R.A. GRAHAM, G.K. STRAUB [Eds.], 227–230, 1983.
2. T. ANTOUN, L. SEAMAN, D.R. CURRAN, G.I. KANEL, S.V. RAZORENOV, A.V. UTKIN, *Spall fracture*, Springer, Berlin, 2002.
3. F. BUY, C. VOLTZ, F. LLORCA, *Thermodynamically based equation of state for shock wave study: application to the design of experiments on tin*, [in:] *Fourteenth Topical Conference on Shock Compression of Condensed Matter*, M.D. FURNISH, M. ELERT, T.P. RUSSELL, C.T. WHITE [Eds.], 547–550, 2005.
4. M.M. CARROLL, A.C. HOLT, *Static and dynamic pore-collapse relations for ductile porous materials*, *J. Appl. Phys.*, **43**, 4, 1626–1636, 1972.
5. L. DAVISON, D. GRADY, M. SHAHINPOOR [Eds.], *High pressure shock compression of solids II. Dynamic fracture and fragmentation*, Springer, New York, 1996.
6. C. DENOVAL, J.-M. DIANI, *Cavitation in compressible visco-plastic materials*, [in:] *Twelfth Topical Conference on Shock Compression of Condensed Matter*, M.D. FURNISH, M. ELERT, T.P. RUSSELL, C.T. WHITE [Eds.], 495–498, 2001.

7. A. DRAGON, H. TRUMEL, *Damage under impact loading. Some modelling challenges*, [in:] *Proc. Fifth High Dynamic Pressure Conference*, C.F.A., 267–283, 2003.
8. D.E. GRADY, *Local inertial effects in dynamic fragmentation*, *J. Appl. Phys.*, **53**, 1, 322–325, 1982.
9. D.E. GRADY, *The spall strength of condensed matter*, *J. Mech. Phys. Solids*, **36**, 3, 353–384, 1988.
10. D.B. HOLTkamp *et al.*, *A survey of high explosive-induced damage and spall in selected metals using proton radiography*, [in:] *Thirteenth Topical Conference on Shock Compression of Condensed Matter*, M.D. FURNISH, N. THADHANI, Y. HORIE [eds.], 477–482, 2003.
11. J.N. JOHNSON, *Dynamic fracture and spallation in ductile solids*, *J. Appl. Phys.*, **52**, 4, 2812–2825, 1981.
12. C. MABIRE, *Transformation polymorphique et fusion de l'étain dans la gamme 0–100 GPa – Etude expérimentale et modélisation*, Doctoral thesis, Université de Poitiers – ENSMA, 1999.
13. T. DE RESSÉGUIER, L. SIGNOR, A. DRAGON, M. BOUSTIE, G. ROY, F. LLORCA, *Experimental investigation of liquid spall in laser shock-loaded tin*, *J. Appl. Phys.*, **101**, 1, 013506, 2007.
14. T. DE RESSÉGUIER, L. SIGNOR, A. DRAGON, P. SÉVERIN, M. BOUSTIE, *Spallation in laser shock-loaded tin below and just above melting on release*, *J. Appl. Phys.*, **102**, 7, 073535, 2007.
15. T. DE RESSÉGUIER, L. SIGNOR, A. DRAGON, M. BOUSTIE, L. BERTHE, *On the dynamic fragmentation of laser shock-melted tin*, *Appl. Phys. Lett.*, **92**, 131910, 2008.
16. G. ROY, *Vers une modélisation approfondie de l'endommagement ductile dynamique. Investigation expérimentale d'une nuance de tantale et développements théoriques*, Doctoral thesis, Université de Poitiers – ENSMA, 2003.
17. L. SIGNOR, T. DE RESSÉGUIER, G. ROY, A. DRAGON, F. LLORCA, *Fragment-size prediction during dynamic fragmentation of shock-melted tin. Recovery experiments and modeling issues*, [in:] *Fifteenth Topical Conference on Shock Compression of Condensed Matter*, M.L. ELERT, M.D. FURNISH, R. CHAU, N. HOLMES, J. NGUYEN [Eds.], 593–596, 2007.
18. S.V. STEBNOVSKII, *Experimental investigation of pulsed stretching of cavitating media*, *J. Appl. Mech. Tech. Phys.*, **39**, 5, 758–761, 1998.
19. R. TEMAM, A. MIRANVILLE, *Mathematical modeling in continuum mechanics*, 2nd Edition, Cambridge University Press, 2005.
20. A.K. ZHIEMBETOV, A.L. MIKHAYLOV, G.S. SMIRNOV, *Experimental study of explosive fragmentation of metal melts*, [in:] *Twelfth Topical Conference on Shock Compression of Condensed Matter*, M.D. FURNISH, Y.M. GUPTA, J.W. FORBES [Eds.], 547–550, 2001.

Received December 4, 2007; revised version June 6, 2008.

---